DISTORTIONAL DEFORMATION OF MATRIX IN OPEN-HOLE TENSION COMPOSITES: EXPERIMENTAL INVESTIGATION

D. Lee[1] and K. Yoshioka[2]

[1]Composite Materials Research Laboratory, Toray Composites (America), Inc.,
Tacoma, WA, USA
Email: dlee@toraytca.com, web page: http://www.toraytca.com

[2]Composite Materials Research Laboratory, Toray Composites (America), Inc.,
Tacoma, WA, USA
Email: kyoshioka@toraytca.com, web page: http://www.toraytca.com

Keywords: Strain invariants, Onset Theory, digital image correlation, homogenization/dehomogenization, open-hole tension

ABSTRACT

Resin strength can be translated to composite strength by quantifying strain invariants of resin according to the Onset Theory. One of advantages that strain invariants could convey is that, as suggested by the term, composite performance is depicted by a pair of intrinsic properties regardless of the stacking sequence. The work here was carried out in order to demonstrate the process of homogenization/dehomogenization between micro- and macro- scale models and ultimately to employ the Onset Theory in the assessment of open-hole tension tests.

For an aerospace-grade material, T800S/3900-2, a series of mechanical tests were carried out: (a) unidirectional 0° tensile tests, (b) unidirectional off-axis tensile tests with angles ranging from 10° to 80°, and (c) unidirectional 90° tensile tests. Experimental evaluation was followed by homogenization/dehomogenization process, which was completed by computational evaluation. Using experimental information obtained from tests (a) to (c), computational analysis at coupon scale was carried out to estimate global strain components. Another analysis at the level of representative volume element was also performed in order to estimate the influence function that relates the strain components in homogenized states to the ones in dehomogenized states. With knowledge of the six strain components and the influence function, the dilatational and distortional strain invariants were computed at a critical point for use as "intrinsic material properties" by which solutions for a wide range of different problems are solved.

This study was extended to further investigation in an effort to replace computational analysis with experimental studies that potentially minimize errors between experimental observation and computational aberration. Since digital image correlation provides accessibility to local strain components at a sub-mm scale, the technique was extensively utilized.

1 INTRODUCTION

The Onset Theory, formerly known as SIFT (Strain Invariant Failure Theory) when it was first introduced [1], has been popular in composite community. It was employed to analyse time-dependent properties of general composite laminates [2] and of open-hole compression [3]. It has been extended to practical applications such as sub-structural components as in Ref. [4] and [5]. Oh *et al*. [6] expanded the theory so that a random fiber array was compared to periodic fiber arrays.

Aforementioned studies, however, heavily rely on computational evaluation in the process of homogenization/dehomogenization to which experimental input data are crucial. Computational analysis such as finite element method often leads to erroneous results due to a number of common reasons: incorrect/lacking data input, sensitivity to operating methods/criteria, sensitivity to meshing and element shape, limited computing power, or even limited capabilities of commercial packages. For this reason, an experimental methodology with the objective of replacement or minimization of the use of computational evaluation was proposed in the study of open-hole tension (OHT) failure prediction.

2 HOMOGENIZATION/DEHOMOGENIZATION

The homogenization/dehomogenization process in the present study follows the original ideas proposed in Gosse and Christensen [1], Pipes and Gosse [7], and Buchanan *et al*. [8]. In these references, finite element analysis (FEA) is chosen as a medium to relate macro-scale strain components to micro-scale counterparts, following Daniel and Ishai [9]. Modeling a composite material, due to its two or more distinctive constituents, often leads to inaccurate estimations if its heterogeneity is not fully considered in modeling. Since modeling heterogeneous phases of a composite laminate is practically unaffordable with typical computational power, the theory suggests that the computational analysis be decomposed into two different analyses, coupon-scale analysis at a macro scale and unit-cell analysis at a micro scale. It is noteworthy that, similar to the aforementioned references, a composite laminate in the present study is limited to an assemblage of multiple laminae in which a lamina is consisted of infinitely continuous fibers impregnated with an isotropic matrix.

The strain invariants are dilatational invariant (J_1) and distortional invariant (J'_2), functions of principal strains ε_1, ε_2, and ε_3:

$$J_1 = \varepsilon_1 + \varepsilon_2 + \varepsilon_3 \tag{1}$$

$$J'_2 = \frac{(\varepsilon_1 - \varepsilon_2)^2 + (\varepsilon_2 - \varepsilon_3)^2 + (\varepsilon_3 - \varepsilon_1)^2}{6} \tag{2}$$

The physical meaning of each invariant is that J_1 represents volumetric change of a solid body under external deformation whereas J'_2 represents deviatoric change. The two parameters, according to the Onset Theory, can characterize the strength of a material and are intrinsic material properties. Strain invariants of matrix resins in composites can be experimentally extracted under the assumptions that: (1) failure of a composite is purely matrix-dominant, (2) any sign of "yielding" is regarded as the onset of irreversible deformation, and (3) local strain state of matrix within the fiber bed is decidedly indicative of either distortional or dilatational deformation.

The evaluation process for the two strain invariants is briefly given in what follows. J_1 and J'_2 are measured from a series of off-axis tension tests in which unidirectional composite coupons with fibers aligned at a certain angle with respect to the loading axis are loaded in tension until fracture, at which point the failure strain is measured. It must be noted that the geometry of a coupon (typically 152.4 × 19.05 mm^2 in gage section) allows no single fiber clamped by both test grips so that composite failure is solely driven by matrix failure. Although testing a wide range of fiber orientation angles (10° to 90° with an increment of 5°-10°) is preferred, the Onset Theory suggests that 10° test for measuring critical distortional invariant and 90° test for critical dilatational invariant should be sufficient. For evaluating the distortional invariant of fiber, 0° tension testing is carried out. The strain at failure measured from the tests above is then fed to FEA models of off-axis tension as a boundary condition and local strain components are measured. In a separate FEA model where a representative volume element (RVE) is modeled, magnification numbers that relate prescribed strain input to strain outcome, known as influence functions, are evaluated. From six mechanical loading conditions, a 6×6 mechanical influence function is extracted whereas a 1×6 thermal influence function is extracted from one thermal loading condition (see Ref. [8] for more details). The influence functions obtained from the RVE analysis are then incorporated into the FEA coupon models to evaluate "true" local strain components. Upon building a RVE model, two fiber arrays are typically used: the rectangular array and the hexagonal array. Random arrays can be considered as in Ref. [6] but consideration of random fiber arrays is beyond the scope of the present study. Each type of arrays produces two sets of influence functions since there are two constituents.

3 MODIFICATION OF EVALUATION PROCESS

In the course of the evaluation process authors encountered a number of issues especially with the computation. Some stemmed from limited experimental accessibility to material properties (*e.g.*, out-of-plane Poisson's ratio of fiber), which is fundamental to make material libraries as input for FEA, and others pertained to the FEA or the commercial package authors used. These causes can be

practically impossible or at the least labor-intensive to fix. At Toray Composites America, Inc. (TCA hereafter), in an effort to minimize the use of computational analysis, experimental studies were emphasized so that inputs and outcomes were more experimentally-based and free from dependency upon numerical results. Assuming digital image correlation (DIC) provides strain measurement that is equivalent to that which FEA provides, DIC can eliminate the use of FEA from the evaluation process.

The experimental setup is shown in Figure 1. The setup consists of two DIC systems, a test frame, a four-lamp white-light lighting system, and three computers as hosts to the two DIC systems and the test frame. A first DIC system records images of the front face (*xy* plane) and another DIC system records images of an edge (*yz* plane) as the off-axis specimen is being loaded. From these two DIC systems, five local strain components, ε_{xx}, ε_{yy}, ε_{zz}, γ_{xy}, and γ_{yz}, are measured as a function of applied stress. The sixth strain component, γ_{zx}, is not possible to measure with the current experimental setup and was simply assumed to be zero since the fibers in *zx* plane are aligned in an orthonormal direction (*x*-axis in this setup). By combining this assumption with the fact that DIC offers full-field strain distributions, the dual-DIC system can measure all six local strain components in replacement of FEA.

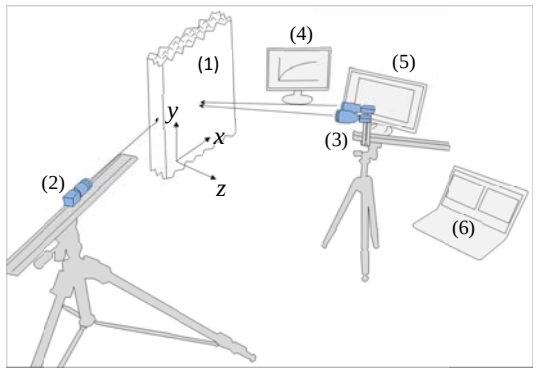

Figure 1. The proposed dual-DIC system experimental setup for off-axis tension test in the present study: (1) specimen, (2) DIC system 1, (3) DIC system 2, (4) strain history from strain gage installed on the back face, (5) strain histories from DIC system 1, and (6) strain histories from DIC system 2.

With this setup, off-axis tension tests for various fiber-orientation angles were carried out from 10° to 90°. Some of the strain histories measured by the dual-DIC system for the angle 32.5° are measured against that by strain gage as shown in Figure 2. It is clear that one of the major strain components, ε_{yy} (in-plane normal strain in loading axis), is measured consistently to be the same value by various methods. This implies that the three testing methods produce legitimate strain values and the specimen alignment is correctly made with respect to the three testing methods.

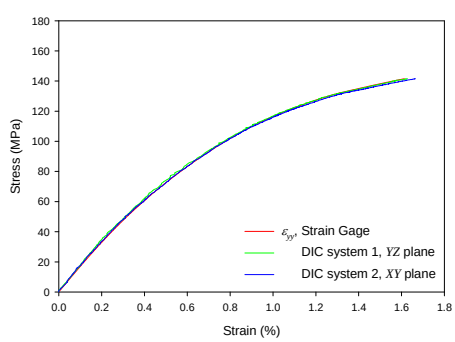

Figure 2. Stress-global strain histories for a 32.5° off-axis tension specimen tested in the present study. The normal strain (ε_{yy}) histories in the loading axis from three different sources are nearly equal.

Strain fields for the same specimen computed by a pattern-tracking algorithm, 3D-VIC™ (Correlated Solutions, Inc., SC, USA), are shown in Figure 3. Images from Figure (a) to (c) were photographed 0.1 second before the image of Figure (d) that is the failed specimen. A reference line for the fracture point shows that strain is highly concentrated at a location that is the eventual location of fracture. Local strain components were measured at this location at this load level.

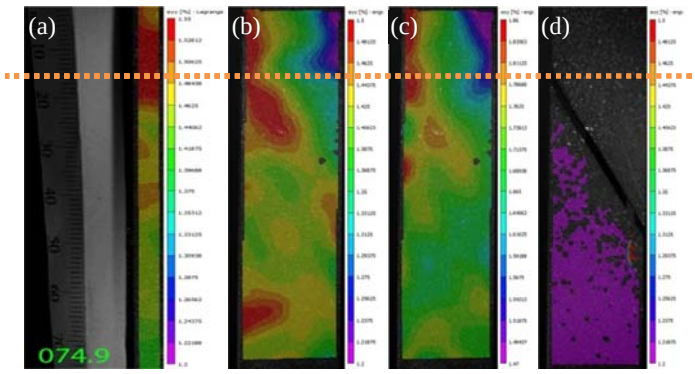

Figure 3. Specimen images for a 32.5° off-axis tension specimen taken by DIC systems 1 and 2: (a) ε_{yy} on *yz* plane, (b) ε_{yy} on *xy* plane, (c) γ_{xy} on *xy* plane, and (d) fractured specimen. Images (a) - (c) were photographed at the same time and time interval between images (a-c) and (d) was 0.1 second. Note that a dotted line was drawn for reference indicating the fracture point.

As illustrated in Figure 1, five local strain components were measured at the fracture point. Stress-strain curves for the 32.5° off-axis tension specimen are shown in Figure 4. A few observations are made in Figure 4. Similar to the case of γ_{yz}, the shear strain on *yz* plane was measured as nearly zero due to the fiber orientation in the plane. Another notable observation is that the shear strain measured from the front face, γ_{xy}, is larger than the normal strain in the loading axis. This is due to the fiber orientation not being aligned in the loading axis. This tendency decreases as the angle increases. For all angles the two major contributors in computing principal strains are ε_{yy} and γ_{xy}. The third contributor is ε_{xx} whose physical meaning is deformation in lateral direction. Since the tension tests carried out in the study are uniaxial it is correct to have negative ε_{xx} values (*viz*., lateral contraction) due to the Poisson's effect. The data points at failure were collected to compute the strain invariants.

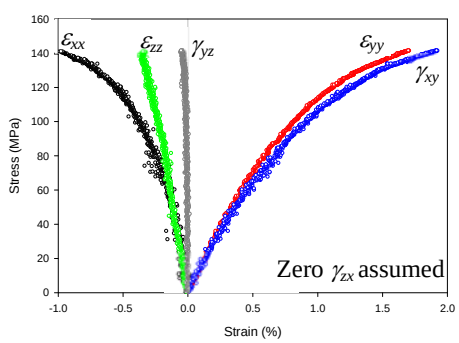

Figure 4. Stress-local strain histories for a 32.5° off-axis tension specimen tested. All strain components are measured at the fracture point.

The computed strain invariants for various angles were closely inspected and dominance of each was examined in a given angle range. The distortional invariant is dominant up to 32.5° and abruptly drops at higher angles whereas the dilatational invariant becomes dominant past 35° and peaks at 60°.

In other words, for smaller-angle off-axis tension (10° to 32.5°), distortional deformation is the main cause for the failure whereas dilatational failure is more dominant for larger angles (35° to 90°).

4 STUDY OF OPEN-HOLE TENSION

In order to implement the developed theory in a practical situation, a number of test subjects were considered for the investigation. Due to a great deal of computation and experimentation anticipated, engineering problems that engineers encounter on a daily basis and that are of simple geometry and dimensions yet that could elevate complexity in analysis were envisioned for the candidates. After a series of benchmark tests, open-hole tension (OHT) test was selected for the current study, which is capable of producing straightforward data (*e.g.*, failure stress) but also complex and even confounding results (*e.g.*, near-hole nonlinearity, untimely local failure, *etc*.) when it is studied in greater detail.

4.1 Material Selection and Preparation

An aerospace-grade material, T800S/3900-2 manufactured at TCA, was selected for the present study. From the previous study, the material was found to be elastic, that is, the onset of irreversible damage coincides with the final failure. Therefore it is aptly categorized into materials that the Onset Theory is limited to cover: *SIFT model covers only the onset of significant irreversible damage, not its propagation if failure is not instantaneous* [10]. The critical dilatational and distortional strain invariants for T800S/3900-2 were found to be 0.02489 and 0.03434, respectively (from the previous chapter). These values will be measured against strain invariant distributions in a FEA OHT model in order to judge the failure of OHT specimen later.

Quasi-isotropic OHT coupons were hand-laid up, debulked, cured, and machined at TCA following typical procedures compliant with the industry-standardized processes and specifications such as ASTM D5766. However, the stacking sequence was chosen so that 0° plies were placed in the mid-plane of each specimen as opposed to ASTM D5766 in which 90° plies are instructed to be placed in mid-plane during layup. Although the tendency is less significant if ply thickness is low, Xu *et al*. argued [11] that quasi-isotropic layups with 0° plies in the mid-plane showed higher initial failure load as well as higher peak load for compact tension specimens, accompanied with a smaller damage zone than those with non-zero plies in mid-plane.

4.2 Experimental Studies

Ten specimens machined from two panels were tested. Black-and-white speckles were patterned on one side in order to enable DIC evaluation and strain gages were installed on the other side to ensure that they would not influence DIC readings. Collecting data from strain gages and DIC pattern simultaneously allows monitoring of local strain gradients as well as global strain gradients. Unlike the strain gage that provides strain measurement at only one point, DIC analysis offers a full-field measurement by which one can have flexibility of measuring strain over the entire region of interest (ROI). However, due to the amplitude of the noise floor of the DIC signal, DIC only measures strain effectively beyond 100 $\mu\varepsilon$ whereas strain gages have virtually no limitation. Therefore, for a study in which measuring local strain gradients and global strain gradients is sought, use of both DIC and strain gages is preferred. Depending on their locations, two types of strain gages were used, namely, Type I and Type II. Type I gages were affixed 90 mm away from the hole center to monitor far-field strain whereas Type II gages were affixed immediately adjacent to the hole edge (~1.6 mm) to monitor near-hole strain.

Strain gage measurements for two different specimens are compared in Figure 5, along with DIC measurement for one of the two. Type I gage measurements of far-field strain for both specimens are nearly identical and only show linear behavior prior to final failure. On the other hand, Type II gage measurements of strain in the vicinity of the hole clearly show nonlinearity for both specimens. Note that the plateau beyond ~3% of strain is not actual strain measurement but caused by errant signal due to the premature failure of strain gage. At a given load level, Type II gage measurements are much higher than Type I gage measurements since the strain is measured in a stress-concentrated region. Of special interest is what happens at the location of Type I in Figure 5, in which the strain signal shows a

discontinuous "jump" in either the positive direction or negative direction. This discontinuity was also evidenced by DIC measurement (marked by black dots in Figure 5) for which data collection was made near the hole edge, in an equivalent fashion to the Type II gage. Such a discontinuity strongly suggests that OHT specimens tested in this study should have undergone initial ply failure at a low load level. For those specimens tested up to final failure, it was found that σ^{μ} = 626 ± 22 MPa and ε^{μ} = 1.202 ± 0.075% at final failure whereas σ^{ini} = 276 ± 12 MPa (44% of stress at failure) and ε^{ini} = 0.927 ± 0.030% (77% of strain at failure) at initial failure.

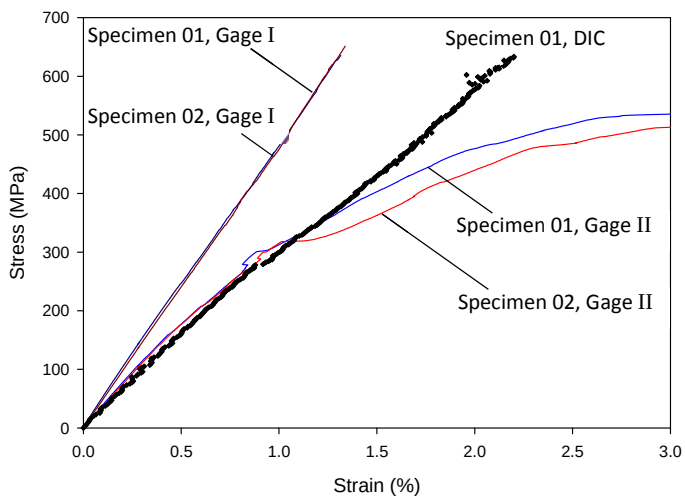

Figure 5. Far-field strain in comparison with near-hole strain.

In order to identify the source of initial failure for OHT specimens, three more specimens were tested but this time they were stopped at a certain load level before which the abrupt strain change was detected. Figure 6 shows stress-strain histories measured by Type II gage for these three specimens in comparison with one of specimens tested previously (the Specimen 01 shown in Figure 5). The three specimens were then machined and polished in order to see the cross-sections near the hole. There are two ways to cut a cross-section: planar cut and edgewise cut. Planar cut shows internal damages of single ply whereas edgewise cut shows those of multiple plies but not in-plane length of damages (See depiction in Figure 6). In the present text, only the edgewise cut will be discussed for brevity.

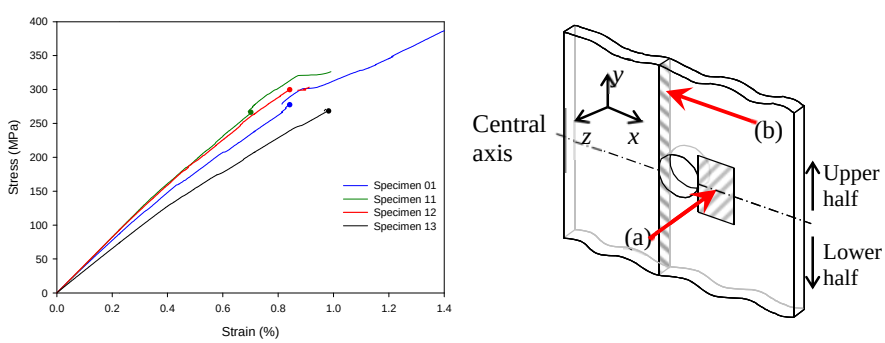

Figure 6. Stress-strain histories for additional specimens tested with marked initial failure and cross-sectional cuts near the hole: (a) planar cut to view *xy* plane and (b) edgewise cut to view *yz* plane.

It is instructive to look at edgewise-cut cross-sections as shown at the top of Figure 7. A total of 22 microcracks were observed over an area of 1.5 × 5.0 mm^2. In the upper half (*i.e.*, left-hand side of the central axis in Figure 7), eight microcracks were found whereas 14 microcracks were found in the

lower half (*i.e.*, right-hand side of central axis). Not only was the number of cracks higher in the lower half, but also the cracks were spread out over a larger area. The number of cracks per ply is also of particular interest. Here is a breakdown for the number of cracks in each ply (top indicates plies above the mid-plane and bottom indicates plies below the mid-plane):

Top +45°:	1
Top 90°:	6
Top -45°:	3
Bottom -45°:	5
Bottom 90°:	6
Bottom +45°:	1

No microcrack was found in any 0° plies. The number of cracks for plies of the same fiber orientation is nearly identical and distribution of cracks in number is nearly symmetric with respect to the mid-plane. All but one crack propagated all the way through a ply but no pair of cracks was found connected across plies. No sign of delamination was found. Not only was the crack length long, but also the number of cracks was found to be higher in 90° plies. In addition, cracks in -45° plies were found to be more than those in +45°. This may be explained by the fact that -45° plies are situated between the major load-carrying 0° plies and the matrix-dominant 90° plies which should induce large shear deformation.

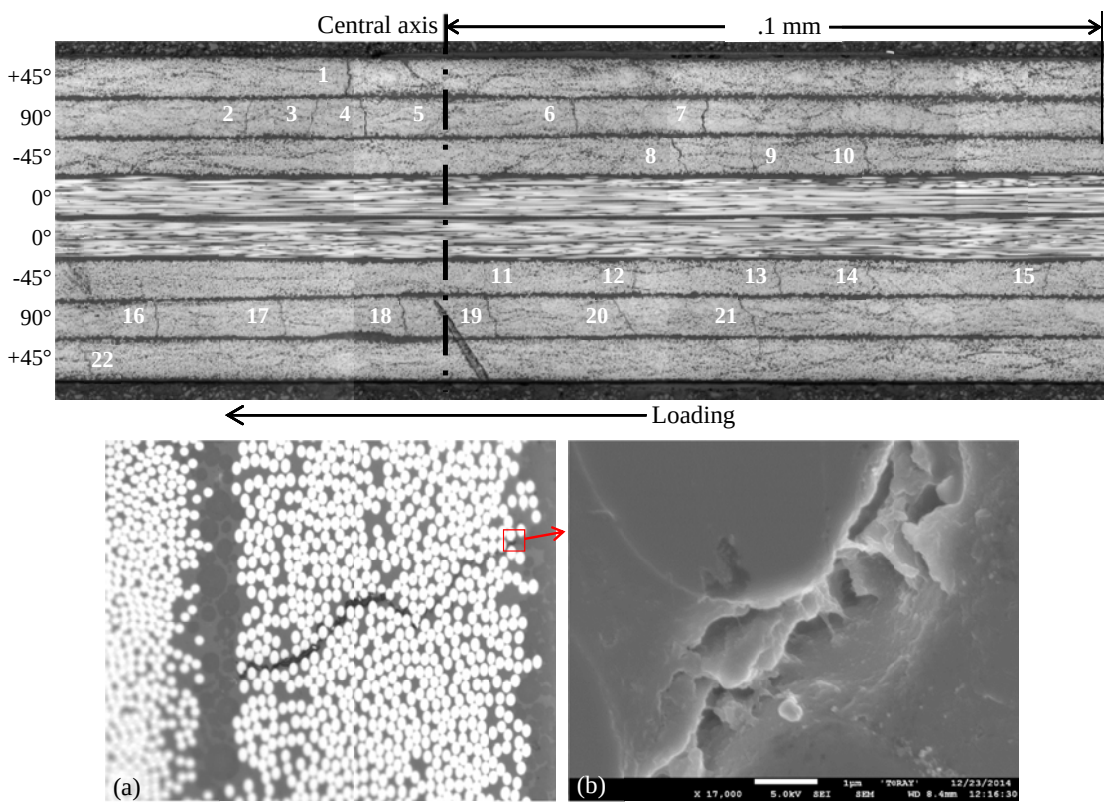

Figure 7. (Top) Through-the-thickness microcracks near the hole by edgewise cut (Shown is Specimen 13). Distance from central axis to the right edge of the image is same as the hole radius. (Bottom) Magnified images of crack no. 8: (a) × 250 and (b) × 17,000. Crack propagation is seen along the fiber-matrix interface in a cohesive manner. It is clear that damage has been made within resin body and remaining resin is still attached to the fiber surface.

To ensure the cracks were propagated within the matrix body, a few selected cracks were

investigated using scanning electron microscope (SEM). One of them, No. 8, is shown at the bottom of Figure 7. Crack growth is apparently along the profile of filaments and no fiber appears damaged. More importantly, no interfacial adhesive failure is observed (*i.e.*, no fiber debonding). Therefore the initial failure of OHT specimens at 40% of failure load is caused by matrix failure.

Specimens 11 and 12 revealed a similar tendency in terms of crack growth pattern, number of cracks, *etc*. However, additional information was drawn, particularly, from Specimen 11. A total of 29 microcracks were observed over an area of 1.4 × 4.0 mm^2 near the central axis, which makes the specimen slightly denser in the number of cracks than Specimen 13. This was anticipated since Specimen 11 had been loaded additional an 18% of total load past the strain abruption whereas only 1% additional loading had been loaded for Specimen 13. Two more microcracks were found in each 90° ply, far from the central axis. One of them was found approximately 5.5 mm away from the central axis and the other was 5.7 mm away from it.

As seen in Specimen 13, the number of cracks for plies of the same fiber orientation is nearly identical and distribution of cracks in number is nearly symmetric. However, unlike Specimen 13, a number of cracks appeared grown half way through a ply. It appears either that such cracks were in the process of propagation but halted at the end of testing or that they changed the path and began growing out-of-plane and thus were not invisible in the micrographs. Another difference is that some of the cracks are connected at the matrix-rich zones but it is uncertain whether they have independently propagated and joined later or one of them has propagated across plies. Similarly to Specimen 13, no delamination was found in Specimen 11.

In summary, the mechanical testing and visual inspection of OHT demonstrated that (1) the specimens, while not detectable in the far field, experience highly localized strain in the vicinity of the hole, (2) the vicinity of the hole, due to the strain localization, undergoes a great deal of deformation, (3) the resulting deformation causes microcracks of the matrix and it was detected by the strain gages and DIC, (4) the microcracks were evidenced by the microscopic and SEM examinations, and (5) the damage of the matrix was found to be cohesive.

4.3 Computational Analysis

In the previous section, experiment of OHT tests ensured that the composite failure was initiated by matrix cracking at a local scale. This was predicted by the Onset Theory such that J_1 and J'_2 of matrix at composite failure reach their critical values before J'_2 of fiber reaches its critical counterparts. Since critical distortional and dilatational invariants for constituents are known (through a series of tests as discussed in Chapters 2 and 3), it would be possible to identify locations where J_1 and J'_2 become equal to or greater than the critical values if the values of J_1 and J'_2 induced by the local principal strain components – in other words, local J_1 and J'_2 – were known. The principal strain components, functions of six strain components, must be evaluated at a micro scale for this task and thus use of computational analysis such as FEA is inevitable. The FEA package used in this study is FEMAP/NASTRAN provided by NEi Software (CA, USA).

Due to the quasi-isotropic coupon layup, fracture could propagate from the hole in four different directions: 0°, 90°, and ±45°. In order to account for such a multi-directional propagation, the model must be built such that crack potentially could grow along one of the prescribed line segments. However, this is not executable with a 2D model while a 3D model would provide all six strain components which are crucial to compute the three principal strains. For this reason, a 3D model was built.

Cohesive zone allows actual separation of elements, if properly modeled, once the displacement reaches prescribed critical values related to mode-I energy release rate (G_{Ic}). There need to be two different mode-I energy release rates: through-the-thickness $G_{Ic}^{(t)}$ and interlaminar $G_{Ic}^{(i)}$. $G_{Ic}^{(t)}$ indicates the maximum allowable value prior to crack initiation through the specimen thickness whereas $G_{Ic}^{(i)}$ indicates the maximum allowable value prior to delamination. The values used in this study are $G_{Ic}^{(t)}$ = 510 N/m [12] and $G_{Ic}^{(i)}$ = 631 N/m [13].

A final load of 40 kN, which is well above the experimental failure load, was applied by incremental increase of load over 25 steps. The result focusing on the vicinity of the hole is shown in Figure 8. As seen in this image, the model with cohesive elements has room to be locally deformed

and/or fractured and therefore noticeable local damage is clearly visible, particularly in the vicinity of the hole. As the major load carrier, 0° plies are subjected to the highly localized stress and they still have capacity to carry the load. However, interlaminar stress at the given load step surpasses the critical value (defined by $G_{Ic}^{(i)}$), which leads to delamination. This was not observed in an OHT model without CZM being applied. Therefore it was concluded that the use of CZM would be necessary to study local damage.

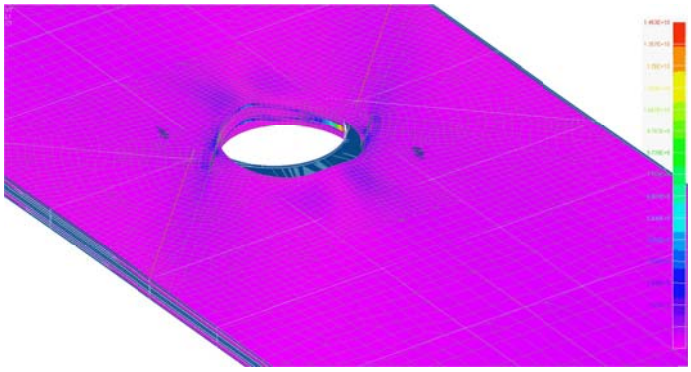

Figure 8. Von Mises stress distribution of an OHT model with CZM. Delamination in the vicinity of the hole is evident. The model consists of 26,576 elements and 52,460 nodes. One ply is one-element thick.

It must be noted that, even with fixed values of G_{Ic}, there is flexibility for interpreting them in a variety of manners. Examples can be found in Extended Schapery Theory [14] or Turon's bilinear mixed-mode cohesive zone model [15]. Since it is beyond the scope of the present study to investigate cohesive zone formulations, a simple bilinear traction-separation law was employed. The bilinear formulation for energy release rate is defined as:

$$G_{Ic} = \int^{\delta_I} \sigma(\delta) d\delta \approx \frac{\sigma_I \cdot \delta_I}{2} \tag{3}$$

assuming the area under the traction–separation (σ_I–δ_I) curve is triangular.

As shown in Figure 5, the far-field stress-strain history from the FEA is plotted in Figure 9 in comparison with experimental data. Up to the load step shown in the figure it is clear that 3D analysis shows a good match in the far field. Due to the initial failure in the vicinity of the hole where matrix cracking was experimentally observed, a jump of strain value was observed. Although it was anticipated that such a strain abruption could not be detected by the current model of FEA, stress-strain history measured near the hole was plotted as also shown in Figure 9. The computational result is in good agreement with values measured by DIC up to ~0.9% of strain after which it departs from the DIC readings. Computational values are still in good agreement with DIC values beyond the discontinuity but not as good as those prior to the discontinuity. Therefore strain readings measured by DIC have been affected by matrix cracking whereas those by computational analysis have not. As a matter of fact, with the current model in which the fiber and matrix are homogenized into a single body, it is impossible to simulate fiber failure and matrix failure separately.

From these observations, it is apparent that the 3D model used in the present study is not built to detect the strain discontinuity, which may not be practically possible since building a dehomogenized model (*viz*., a model with distinctive constituents) at macro level is computationally unaffordable. On the other hand, the model still produced prediction of delamination at a high level of stress, a common source of damage of quasi-isotropic laminate, and can be used for evaluation of strain invariant status.

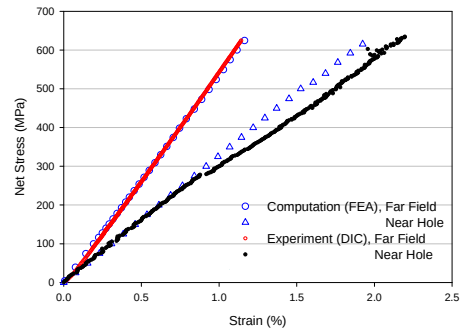

Figure 9. Comparison between experimental data (DIC) and computational data. Computational readings match the experimental readings in the far field whereas they deviate from the experimental readings, especially later stage of the event, at near-hole region.

The current FEA model was unable to simulate the discontinuity of strain since it was built in a homogeneous manner. By implementing the Onset Theory, however, the model can be handled as an assemblage of two distinctive constituents since there are two sets of input data available, for each fiber and matrix as discussed Chapter 2. In the 3D analysis, strain invariants are converted from six strain fields. The J'_2 for the matrix at a given load step is substantially higher than that of fiber. In other words, the matrix is subjected to higher distortional deformation that allows excluding any possibility that fiber fails prior to resin failure, which is in agreement with the experimental observation discussed in Section 4.2. For this reason, distortional failure of fiber will not be discussed from this point forward. Maximum J'_2 was evaluated at each load step with the same 3D model in Figure 10. From Chapter 3, the critical distortional strain invariant for T800S/3900-2 was found to be 0.03434. At a given load level, if J'_2 of the OHT body is lower than this value, the OHT body is considered undamaged whereas the body fails if it is higher. From the plot in Figure 10, J'_2 of the rectangular array becomes higher than the critical value when the load level is approximately 300 MPa but J'_2 of the hexagonal array is still lower at the same load level and it exceeds at the next load step. In other words, an ideal OHT specimen packed with fibers in the rectangular array would have failed at the load level 300 MPa whereas an OHT specimen with hexagonal fiber array would not have failed until the load level reached 325 MPa. The experimental load level at which the initial failure occurred was 276 MPa from Section 4-2, thus the value is in between the load step 300 MPa and the previous step. This is in agreement with the observations from the computational results, especially for the rectangular array. Considering the large increment of load steps (27 MPa in this study) and a scatter of experimental load level (5% of coefficient of variation), the present model is capable of predictions with a high accuracy.

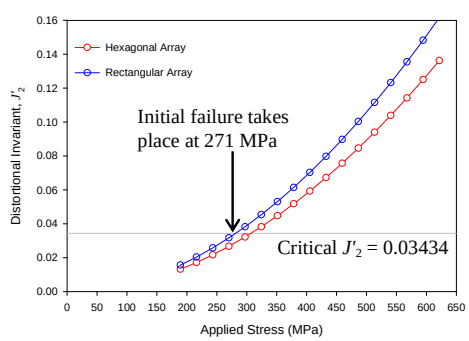

Figure 10. Distortional invariant (J'_2) as a function of applied stress in the OHT analysis.

4.4 Discussion

In the course of theory validation and application, it was found that FEA exhibited certain limitations such as fiber arrays being limited to periodic arrays and/or inability of FEA to handle localized stress/strain among other limitations. In order to study the current problem more reliably, a testing technique, dual-DIC system, was added to the existing testing method, which permitted calculation solely relying on experimental data. Two DIC systems monitor an off-axis tension specimen simultaneously: one monitoring a first plane and the other monitoring a second plane orthogonal to the fist. With this setup in addition to the fact that DIC offers full-field strain distributions, one can measure all necessary local strain components experimentally. Another advantage of this approach is that it can eliminate an FEA unit-cell analysis. The purpose of unit-cell analysis is to compute influence functions that relate local strain components of homogeneous body to local strain components of heterogeneous body to adjust mismatch caused by heterogeneity of composite materials. Experimental data, on the other hand, already reflect heterogeneity since they are phenomenological.

For example, in an off-axis tension test to which a uniaxial loading is applied, both DIC and FEA produced somewhat similar values for two major contributors, ε_{yy} (in-plane normal strain in loading axis) and γ_{xy} (in-plane shear strain on the *xy* plane). However, the third contributor, ε_{xx} (in-plane normal strain perpendicular to the loading axis), was largely different. DIC produced a negative value whereas FEA produced a positive value. For the uniaxial tensile loading, a lateral contraction must be accompanied with longitudinal extension. In other words, both ε_{xx} and ε_{zz} (out-of-plane normal strain perpendicular to the loading axis) should be negative which is in an agreement not with computational data but with experimental data.

5 CONCLUSIONS

The principles of the Onset Theory were adapted in a study of OHT. Instead of using numerical methods, a new technique using a dual-DIC system was employed and the critical strain invariants for a high-grade composite material, T800S/3900-2, were evaluated. In the study of OHT, however, this technique cannot be directly employed due to the technical challenges. For this reason, the influence functions for the material with two hypothetical fiber arrays were computed using unit-cell analyses.

Through a series of OHT tests, it was found that OHT specimens locally failed at a low load level (43% of failure load) within the matrix body and it was hypothesized that this initial failure would be due mainly to cohesive failure of the matrix. It was later confirmed that matrix was indeed damaged cohesively under photographic examination by optical microscopy and SEM.

With the evaluated critical strain invariants and test results of OHT, 3D FEA analysis was carried out for OHT. The analysis was correctly able to identify the stress level at the initial failure especially for the OHT with rectangular fiber array.

REFERENCES

[1] J. Gosse and S. Christensen, Strain Invariant Failure Criteria for Polymers in Composite Materials, *19th AIAA Applied Aerodynamics Conference, Anaheim, CA, June 11-14, 2001*, AIAA-2001-1184.

[2] S.W. Tsai and J.L. Townsley, Methodology for Composite Durability Assessment, *SAMPE Technical Conference, Dayton, OH, September 28-October 2, 2003*.

[3] H. Cai, Y. Miyano and M. Nakada, Long-term Open-hole Compression Strength of CFRP Laminates based on Strain Invariant Failure Theory, *Journal of Thermoplastic Composite Materials*, **22** (1), 2009, pp. 63-81.

[4] R. Li, D. Kelly, and R. Ness, Application of a First Invariant Strain Criterion for Matrix Failure in Composite Materials, *Journal of Composite Materials*, **37** (22), 2003, pp. 1977-2000.

[5] J.-S. Park, M.-J. Kim, H.-K. Hur, and M.-S. Kim, Damage Evaluation with Multi-scale Failure Analysis using Material Degradation Model based on SIFT, *15th Composite Durability Workshop, Ishikawa, Japan, October 17-20, 2010*.

[6] J.H. Oh, K.K. Jin, and S.K. Ha, Interfacial Strain Distribution of a Unidirectional Composite with Randomly Distributed Fibers under Transverse Loading, *Journal of Composite Materials*, **40** (9), 2006, pp. 759-78.

[7] R.B. Pipes and J.H. Gosse, An Onset Theory for Irreversible Deformation in Composite Materials, *17th International Conference on Composite Materials, Edinburgh, UK, July 27-31, 2009*.

[8] D.L. Buchanan, J.H. Gosse, J.A. Wollschlager, A. Ritchey, and R.B. Pipes, Micromechanical Enhancement of the Macroscopic Strain State for Advanced Composite Materials, *Composites Science and Technology*, **69**, 2009, pp. 1974-1978.

[9] I.M. Daniel and O. Ishai, *Engineering Mechanics of Composite Materials*, Oxford University Press, New York, NY, 2006

[10] L.J. Hart-Smith, Bolted Joint Analyses for Composite Structures - Current Empirical Methods and Future Scientific Prospects, *ASTM STP 1455: Joining and Repair of Composites Structures*, 2004, pp. 127-160.

[11] X. Xu, M.R. Wisnom, S.R. Hallett, N. Zobeiry, S. Leslie, A. Poursartip, and R. Vaziri, Stacking Sequence Effects in Over-Height Compact Tension Tests of Quasi-Isotropic Laminates, *19th International Conference on Composite Materials, Montreal, Canada, July 28-August 2, 2013*.

[12] D. Lee, H. Tippur, P. Bogert, Quasi-Static and Dynamic Fracture of Graphite/Epoxy Composites: an Optical Study of Loading-Rate Effects, *Composites Part B: Engineering*, **41** (6), 2010, pp. 462-474.

[13] Toray Technical Manual.

[14] W. Ji, S.P. Sringeri, S. Thorsson, C. Kosztowny, A.M. Waas, M. Rassaian, and S. Liguore, Face-on and Edge-on Impact Response of Composite Laminates, *56th AIAA/ASCE/AHS/ASC Structures, Structural Dynamics, and Materials Conference, Kissimmee, Florida, January 5-9, 2015*, AIAA 2015-0956.

[15] Turon, P. Camanho, J. Costa, and C. Dvila, A damage Model for the Simulation of Delamination in Advanced Composites under Variable-Mode Loading, *Mechanics of Materials*, **38** (11), 2006, pp. 1072-1089.